

Article

Honeycomb-like Hierarchical Porous Carbon from Lignosulphonate by Enzymatic Hydrolysis and Alkali Activation for High-Performance Supercapacitors

Xin Zhang ^{1,2}, Shi Liu ¹, Yuqi Zhao ¹, Haicun Yang ¹ and Jinchun Li ^{1,2,3,*}¹ School of Materials Science and Engineering, Changzhou University, Changzhou 213164, China² National-Local Joint Engineering Research Center of Biomass Refining and High-Quality Utilization, Changzhou 213164, China³ Jiangsu Key Laboratory of Environmentally Friendly Polymeric Materials, Changzhou University, Changzhou 213164, China

* Correspondence: lj999@cczu.edu.cn

Abstract: Porous carbon materials (PCs) were prepared via hydrothermal carbonization from calcium lignosulfonate (CL) based on enzymatic hydrolysis and alkali activation. The effects of enzymatic hydrolysis and different KOH feeding ratios on the structure and electrochemical properties of enzymatic hydrolysis CL (EHCL)-derived PCs were evaluated in detail. The results showed that the EHCL-derived PCs showed a higher SSA than that of CL. When the mass ratio of KOH/EHCL was 3/2, the PCs exhibited a honeycomb-like microscopic morphology with a specific surface area of up to 1771 m²/g and a 3D hierarchical porous structure composed of abundant micropores, mesopores, and macropores. As an electrode in a supercapacitor, the highest specific capacitance was 147 F/g at a current density of 0.25 A/g, and it maintained 78% of the initial value at a high current density of 10 A/g. The excellent electrochemical cycle and structural stability were confirmed on the condition of a higher capacitance retention of 95.2% after 5000 times of galvanostatic charge/discharge. This work provides a potential application of CL in high-performance supercapacitors.



Citation: Zhang, X.; Liu, S.; Zhao, Y.; Yang, H.; Li, J. Honeycomb-like Hierarchical Porous Carbon from Lignosulphonate by Enzymatic Hydrolysis and Alkali Activation for High-Performance Supercapacitors. *Energies* **2023**, *16*, 3824. <https://doi.org/10.3390/en16093824>

Academic Editors: Huang Zhang and Yuan Ma

Received: 18 March 2023

Revised: 20 April 2023

Accepted: 27 April 2023

Published: 29 April 2023



Copyright: © 2023 by the authors. Licensee MDPI, Basel, Switzerland. This article is an open access article distributed under the terms and conditions of the Creative Commons Attribution (CC BY) license (<https://creativecommons.org/licenses/by/4.0/>).

Keywords: calcium lignosulfonate; enzymatic hydrolysis; alkali activation; hierarchical porosity; supercapacitors

1. Introduction

As a basic demand for social progress and development, the energy demand in transportation, electronics, smart devices, and other fields of the world has significantly increased in recent years, and new energy technologies have gradually become the focus of researchers [1,2]. Relatively clean energy conversion technologies such as new batteries and supercapacitors are considered to be the key to solving the future energy crisis [3,4]. Among these, supercapacitors with higher power densities, high-efficiency energy storage systems, and excellent durability have attracted relatively strong attention, and have been widely used in electronic equipment in daily life, national defense, and military fields [5,6]. These green and sustainable energy storage devices can effectively avoid the excessive consumption of fossil raw materials—especially high-efficiency, environmentally friendly, and low-cost supercapacitors with excellent performance—because most carbon source materials are currently related to fossil fuels such as ethanol, acetylene, and pyridine [7,8]. Biomass energy has a large storage capacity, low development cost, and low environmental pollution in nature, and it is crucial to switch to bio-renewable carbon sources [9]. Generally, the performance of supercapacitors is mainly determined by their electrode materials, and high-performance electrode materials can endow superelectric devices with a higher energy density [10]. Carbon materials have been the research focus in the field of electrode materials due to their high stability and preferred electrical conductivity. Importantly,

their structural adjustability makes it possible to obtain porous carbon materials with a high specific surface area (SSA) and an ideal pore structure [11–13]. Compared with other new carbon-based electrode materials (nano-onions, nanotubes, nanospheres, aerogels, graphene, etc.), porous carbon has the advantages of a wide source of precursors, designability of diversified morphology, relatively simple preparation process, and low cost, resulting in the main direction for the future development of supercapacitor electrode materials [14–16].

Compared with fossil fuels and their derivatives, the use of sustainable, inexpensive, and environmentally friendly bio-based materials to prepare porous carbons is more attractive [17,18]. Biomass materials as new energy are mainly composed of polysaccharides, lignin, proteins, chitin, nanocellulose, and wood, which can be modified by physical or chemical methods to prepare renewable carbon materials in the presence of an activator [19–23]. As an amorphous polymer, lignin is a type of natural biomass fuel with abundant reserves on earth, and its molecular structure endows it with a high carbon content. At present, lignin and its derivatives are the primary by-products of the paper industry, with an amazing output in the world every year. The main treatment method is to directly burn it to recycle new energy, but this also causes serious environmental pollution [24,25]. The molecular unit of lignin is based on hydroxyphenylpropane, which is linked by carbon–carbon bonds or other chemical bonds [26]. This type of high-carbon macromolecular structure makes lignin widely used in the field of flame-retardant polymers [27,28]. Moreover, the chemical composition of lignin includes three propane-type phenol units, and this macromolecule with a high carbon content is an ideal precursor for preparing porous carbon materials. In recent years, low-cost lignin-derived carbon materials have also been used in dye adsorption, titanium dioxide capture, and energy storage technology to explore potential ways to solve environmental and climate problems [29–31]. Compared with pure lignin and lignosulfonates, the enzymatic hydrolysis of lignin has no influence on its main chemical structure; the carbon skeleton can be doped with some nitrogen and oxygen at the same time, which has been demonstrated to be an effective approach to enhance the hydrophilicity and electrochemical performance of lignin-derived carbon materials [32,33].

Unlike the metal oxide click materials used in most pseudocapacitors, carbon-based materials mostly feature double-layer capacitance, in which electrostatic charges are accumulated and released in the electric double-layer formed at the interface between the electrode and the electrolyte [34–36]. This type of electric double-layer capacitor (EDLC) is expected to overcome the poor cycle stability and poor conductivity of pseudocapacitors, and has a high-cost performance [37]. Nevertheless, SSA and hydrophilicity are important indicators of EDLC electrode materials, and hydrophilic porous structures with a high SSA can increase the contact area of electrodes and electrolytes and provide enough reservoirs and smooth channels for electrolyte diffusion and ion transport [38,39]. Although traditional porous carbon materials (PCs) have a high specific surface area, the pore size distribution (0.5–1.1 nm) of their microporous structure is usually narrow, which leads to a poor rate performance due to the nanoporous structure, severely limiting the ion diffusion [40]. Materials such as carbon nanotubes (CNTs), graphene, and carbon fibers (CFs) have been often used as a support for flexible electrode materials, and the surface needs to be chemically modified to reconstruct a suitable porous structure [41–43]. In terms of improving the double-layer capacitance rate performance, novel PCs with hierarchical porosity have more advantages in the field of double-layer capacitors than those with a uniform pore size distribution [44]. Specifically, macropores can provide reservoirs for ion buffering, mesopores can shorten the distance that ions are transported to internal channels, and micropores can provide more ion accumulation sites. The preparation of PCs with hierarchical porosity by the template method is the common method reported in the literature. The template materials involved include zeolite, silica, and metal–organic frameworks [45–47]. However, the complex synthetic steps and expensive price of these template materials make them unable to be mass-produced.

It has been fully proved that chemical activation also provides a facile and effective method to obtain porous structures with a high SSA. For example, under an inert gas environment, carbon precursors can be mixed with KOH, K_2CO_3 , etc., and then pyrolyzed to produce a porous structure through multiple chemical and physical reactions at high temperatures [48]. Among them, template-free KOH pore-forming technology is regarded as relatively easy and inexpensive to produce a carbon material with hierarchical porosity, in which the pore structure and electrochemical properties tend to be more dependent on the precursor and KOH feed ratio [49]. In addition to the type of activator and activation process parameters, the intrinsic structure difference of precursors also leads to the diversification of the PCs' microstructure during carbonization [50,51]. Generally speaking, precursors with smaller molecular weights are beneficial to the formation of carbon materials with a high porosity, improving the graphitization degree when under direct carbonization. The decomposing enzyme contained in the bacterial strain can effectively reduce the molecular weight of lignin. It has been reported that the biotransformation of lignin to lipids, adipic acid, and polyhydroxyalkanoate can be easily realized in the presence of some bacteria [52].

Calcium lignosulfonate (CL), as the main by-product of the paper industry, is often used as a multi-component polymer anionic surfactant. CL may also be preferred as a more ideal precursor of porous carbon materials than lignin, which endows it with a potential application in porous carbon electrode materials for supercapacitors [53]. A large number of natural small molecular compounds and calcium ions in CL act as a template and activating synergist, respectively, which promotes the development of the pore structure in PCs [54]. Laccase is a type of commonly used lignin-degrading enzyme, which is widely distributed in plants, insects, fungi, and bacteria. Enzymatic hydrolysis lignin shares a similar chemical composition to that of native lignin, and nitrogen and oxygen can be doped to the carbon skeleton through biological fermentation during the enzymatic hydrolysis process, thus enhancing the hydrophilicity of carbon materials and introducing pseudocapacitance [55]. For CL, in addition to the above advantages, the deep degradation of CL by laccase can also improve the uniformity of calcium ion distribution in CL, obtaining a more ideal pore structure.

Hence, in this work, hierarchical PCs were prepared from low-cost calcium lignosulfonate (CL) by combining enzymatic hydrolysis and KOH activation. Firstly, CL was enzymatically hydrolyzed with laccase to depolymerize the macromolecules and promote carbonization. Secondly, the enzymatic hydrolysis CL (EHCL) obtained was carbonized in the presence of KOH to generate 3D hierarchical PCs composed of abundant cross-linked macropores with incalculable micropores and mesopores based on the template-free method. The prepared PCs were subsequently used as EDLC electrodes in liquid electrolytes, and the effect of enzymatic hydrolysis and the lignin/KOH feed ratio on the microstructure and electrochemical performance was investigated in detail. This work promotes the application of low-cost biomass resources in supercapacitors. The preparation of 3D-structured hierarchical PCs is an ideal approach to broaden the application field of lignin and its derivatives.

2. Materials and Methods

2.1. Materials

The calcium lignosulphonate (CL; industrial grade) was supplied by Gongyi Shengshi Refractories Co., Ltd. (Gongyi, Henan, China). Potassium hydroxide (AR), sulfuric acid (98 wt%), and hydrochloric acid (36–38 wt%) were purchased from Sinopharm Chemical Reagent Co., Ltd. (Shanghai, China). Laccase (99 wt%) was bought from Tianjin Mingshi Biotechnology Co., Ltd. (Tianjin, China). Poly(vinylidene fluoride) (PVDF; 9000 HD) was supplied by Arkema Inc. (Serquigny, France). All raw materials and reagents were used directly without any pretreatment.

2.2. Preparation of Enzymatic Hydrolysis Calcium Lignin (EHCL)

In a 500 mL three-necked flask, 10 g of CL was mixed with 100 mL of HCl (pH = 4), and then 1 mL of laccase was added. After full dissolution, the solution was continuously stirred at 50 °C for 6 h under nitrogen protection. After the reaction, the product—enzymatic hydrolysis calcium lignin (EHCL)—was filtrated and repeatedly washed with ultrapure water, followed by drying to a constant weight at 80 °C.

2.3. Preparation of KOH-Activated PCs

In an alumina ark, 3 g of EHCL and 50 mL of 5 wt% H₂SO₄ were introduced. After thorough mixing, the ark was placed in an oven at 180 °C for 24 h for pre-carbonization and then naturally cooled to room temperature to afford hydrochar. After being washed and purified by ultrapure water, 2.4 g of acid-treated EHCL hydrochar and KOH (KOH/EHCL = 1:2, 2:3, 1:1, and 3:2) were mixed and then evenly ground in a planetary ball mill. During the grinding process, about 50 mL of ultrapure water was added to form a uniform slurry. Subsequently, under nitrogen protection, the slurry was heated up to 300 °C and kept for 2 h, and then further heated up to 800 °C at 5 °C/min. After carbonization at 800 °C for 3 h, the residual samples were cooled, washed with HCl (4 mol/L) several times, and thoroughly washed with ultrapure water to neutrality. The prepared PCs were completely dried at 120 °C in an oven and named EHCL-Ka, EHCL-Kb, EHCL-Kc, and EHCL-Kd. Meanwhile, CL was directly activated with KOH under a mass ratio of 3/2 (KOH/CL) to prepare the comparative sample, which was named CL-K.

2.4. Preparation of Solid Electrolyte

The supercapacitor electrodes were prepared according to the method reported previously [32]. Typically, the EHCL-Ks ('s' indicates a, b, c, and d), poly(vinylidene fluoride) (PVDF), and acetylene black (mass ratio of 8:1:1) were mixed with 10 mL of ethanol to form a homogeneous slurry and then molded together with foamed nickel at 3 mPa. Finally, the volatile product was thoroughly removed in a vacuum oven at 100 °C to obtain the solid electrolyte.

2.5. Characterization

Fourier transform infrared (FTIR; Avatar 460, Thermo Nicolet, Madison, WI, USA) was performed to confirm the chemical composition at a frequency range of 500–4000 cm⁻¹ in transmission mode. Raman spectra (Raman, DXR, Thermo Scientific, Waltham, MA, USA) and X-ray diffraction (XRD; XRD-6000, Shimadzu, Kyoto, Japan) were used to confirm the physical structures. The microstructure observation of carbon materials was performed using scanning electron microscopy (SEM; JSM-6360LA, JEOL, Tokyo, Japan). The SSA values of different carbon materials were determined by nitrogen adsorption–desorption at 77 K on a TriStar II 3020 micropore analyzer (Micromeritics, Norcross, GA, USA) after degassing at 150 °C for 12 h. The SSA and PSD values were calculated based on the Brunauer–Emmett–Teller (BET) density functional theory (DFT) method. The average molecular weights of CL and EHCL were determined by gel permeation chromatography (GPC). A sodium nitrate aqueous solution of 0.1 mol/L and sodium polystyrene sulfonate with a narrow distribution were used as the eluent and reference, respectively.

The electrochemical performance measurement was tested using three-electrode systems under ambient conditions on an electrochemical workstation (CHI660E, Shanghai Chenhua Instruments, Shanghai, China), and the cyclic voltammetry (CV), galvanostatic charge/discharge (GCD), and electrochemical impedance spectroscopy (EIS) curves were recorded. The mass loading of the active material in the PC electrode was about 1.0 mg/cm². A total of 6 M KOH and platinum foil containing Hg/HgO were used as the reference and counter electrode, respectively, and formed a three-electrode system with the PC electrode. The CV curves were recorded at an operating voltage from –0.2 to –1 V, EIS was conducted in the frequency range of 10 mHz to 100 kHz, and the GCD curves were recorded on a LAND CT2001A tester. The gravimetric specific capacitance was obtained from the GCD

tests via the following equation (Equation (1)), where C was the specific capacitance (F/g), I was the discharge current (A) during the GCD test, Δt was the discharge time, ΔV was the potential change during the discharge, and m was the weight of the PC electrode.

$$C = (I \times \Delta t) / (\Delta V \times m) \quad (1)$$

The electrochemical performance of EHCL-Kd was also evaluated by a two-electrode system using an assembled symmetrical supercapacitor. In a coin cell, two identical working electrodes were separated by a filter paper separator (the active material load of a single electrode is 3 mg). The electrochemical performances were also determined by the CV and GCD results. The specific capacitances were calculated using the following equation (Equation (2)), where m was the mass of the loading of EHCL-Kd on a single working electrode.

$$C = 2(I \times \Delta t) / (\Delta V \times m) \quad (2)$$

The energy density E (Wh/kg) and power density P (W/kg) were calculated based on the following equations (Equations (3) and (4)).

$$E = C \times \Delta V^2 / (2 \times 4 \times 3.6) \quad (3)$$

$$P = 3600 \times E / \Delta t \quad (4)$$

3. Results

SEM characterization was carried out to investigate the morphology of the different precursors and carbon materials. As seen in Figure 1a,b, the surface of CL presented an uneven, porous (1–4 μm), and rough morphology, and the CL-derived hydrochar presented many broken carbon balls (Figure 1c,d). After enzymatic hydrolysis, EHCL exhibited a relatively smooth surface with an obviously decreased particle size (Figure 1e,f), and the structure of the EHCL-derived hydrochar was significantly looser compared with that of CL (Figure 1g,h). The hydrochar derived from CL and EHCL exhibited dramatically different microstructures, which indicated that enzymatic hydrolysis had a significant effect on the carbonization process. The EHCL-derived hydrochar was almost completely composed of carbon blocks with a regular carbon skeleton, higher surface area, and smooth surface. The microstructures of CL-K and EHCL-Kd were further compared (Figure 1i–l). CL-K exhibited collapsed structures with irregular holes, and the inner surface of these holes was distributed with individual small holes with irregular structures (Figure 1i,j). Compared with the EHCL-derived carbon materials, the particles of EHCL-Kd were further loosened and refined, and the single particle showed a distinct porous structure (Figure 1k). In the high-resolution image (Figure 1l), EHCL-Kd presented a honeycomb-like microstructure with a smooth pore wall, interconnected pores, and hierarchical porosity. Macropores with diameters of 100–450 nm could be observed from the high-resolution SEM images, and were interconnected by a large number of mesopores with diameters of 20–80 nm. The SEM results directly demonstrated that enzymatic hydrolysis combined with an alkali catalysis was the necessary step to convert CL into 3D hierarchical porous carbons through the hydrothermal carbonization process.

The morphology and microstructure of EHCL-Kd were also analyzed by the TEM method, and Figure 2 shows the TEM images of EHCL-Kd with different magnifications. In Figure 2a, EHCL-Kd presents a two-dimensional gauze-like structure similar to graphene, which promoted the formation of mesopores. In Figure 2b, at a higher magnification, parallel graphene lattice stripes can be observed around the mesopores, which were formed from the aromatic ring of CL at a high temperature. This two-dimensional structure rich in nanopores could optimize the transport and storage of ions, and the graphite structure could improve the electron transport ability of PCs.

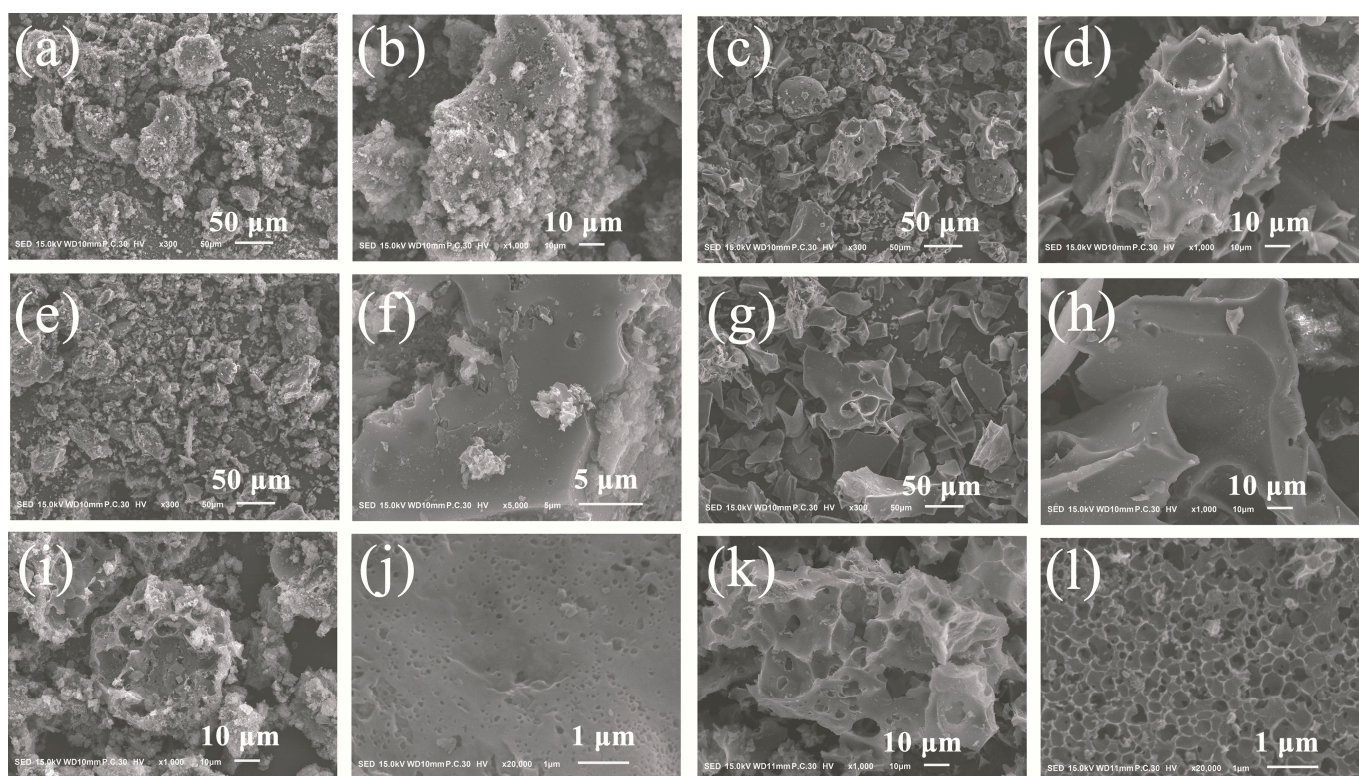


Figure 1. SEM images: (a,b) CL; (c,d) hydrochar derived from CL pre-carbonized at 180 °C; (e,f) EHCL; (g,h) hydrochar derived from EHCL pre-carbonized at 180 °C; (i,j) CL-K; and (k,l) EHCL-Kd.

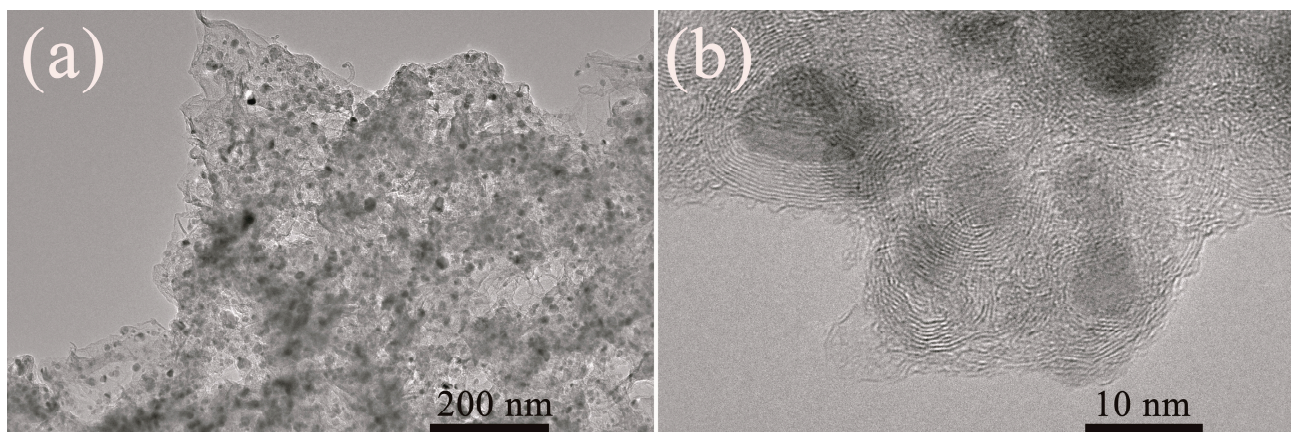


Figure 2. TEM images of EHCL-Kd: (a) 50,000 and (b) 1,000,000 magnifications.

The above morphology analysis results indicated that the carbon skeleton of EHCL-Kd contained abundant mesopores and micropores as well as interconnected macropores, in which the micropores and mesopores were evenly distributed on the surface of the macropores. This unique 3D structure with a high SSA enlarged the electrode/electrolyte contact interface for EDLCs. Importantly, with the contribution of hierarchical porosity, the high SSA could significantly improve the electrochemical performance. Micropores, mesopores, and macropores play a role in promoting charge accumulation, accelerating ion diffusion, and providing storage buffering space for ions.

The changes in the chemical groups of CL before and after enzymatic hydrolysis were compared by FTIR, and the results are shown in Figure 3a. For CL, 3370 cm^{-1} was the O–H stretching vibration; 2949 and 2837 cm^{-1} belonged to the antisymmetric and symmetric stretching vibration of C–H in the methoxy group, respectively; and the benzene

ring skeleton vibration gave two peaks at 1595 and 1515 cm^{-1} . The area near 1421 cm^{-1} was related to the C-H bending vibration. The two sharp peaks at 1163 and 1044 cm^{-1} corresponded with the sulfonic acid group, and the C-S stretching vibration was found at 641 cm^{-1} . In the spectra of EHCL, the characteristic peak corresponding with O-H near 3400 cm^{-1} still existed after enzymatic hydrolysis, and the characteristic peaks at 2937 and 2844 cm^{-1} corresponding with C-H became more obvious. Meanwhile, a new peak of C=O appeared at 1699 cm^{-1} , which was mainly from the laccase molecule. The peak at 1600 cm^{-1} was assigned to the benzene ring skeleton connected with the polar groups; 1508 cm^{-1} was the superposition peak of the benzene ring, C=C, and O-H. The area in the range of 1320–1470 cm^{-1} was the overlapping peaks of a series of groups, mainly including the O-H bending and the in-plane bending of C-H in C=CH. The peak at 1217 cm^{-1} corresponded with the asymmetric stretching of =C-O-C connecting the benzene ring, and 831 cm^{-1} was caused by the out-of-plane vibration of C-H in the multi-substituted benzene ring. Comparing the FTIR spectra of CL and EHCL, it was found that characteristic peaks such as C-H, the benzene ring, and C-O related to organic components in EHCL were more obvious. Therefore, it could be speculated that enzymatic hydrolysis led to the degradation of chlorine and a reduction in the average particle size. It could be seen from the GPC results of CL and EHCL that enzymatic hydrolysis reduced the average molecular weight of CL by about 11%, and the polydispersity index decreased from 1.15 to 1.05 (Figure S1).

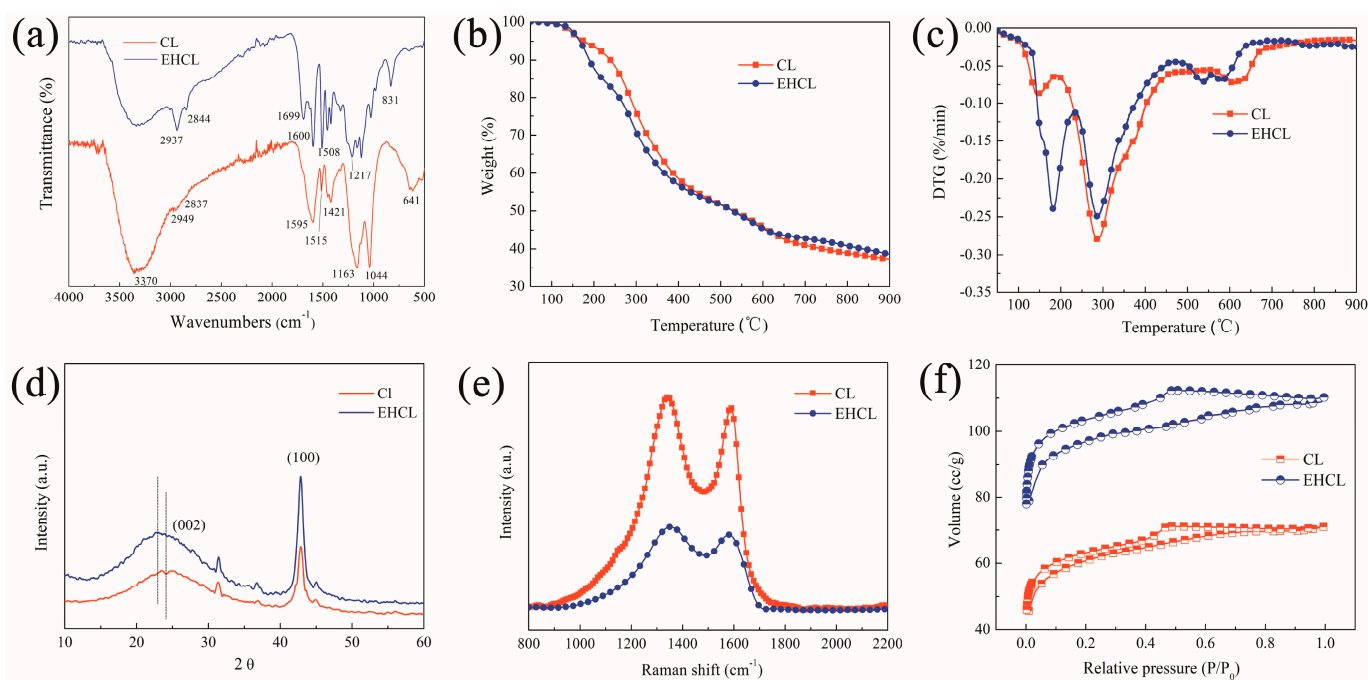


Figure 3. (a) FTIR spectra, (b) TG curves, and (c) DTG curves of CL and EHCL; (d) XRD patterns, (e) Raman spectra, and (f) N_2 adsorption–desorption isotherms of carbon materials derived from CL and EHCL.

The differences in the carbonization process of CL and EHCL were compared by TGA (Figure 3b,c). In general, the activation degree of the lignin chemical bonds in CL was relatively high, so the TGA curve had a wide range of weight loss at 100–900 $^{\circ}\text{C}$, containing three stages [56]. The first stage, lower than 200 $^{\circ}\text{C}$, was mainly due to the removal of moisture in the CL, which resulted from the cleavage of some hydroxyl-containing side chains. The violent decomposition stage after 200 $^{\circ}\text{C}$ lasted until about 490 $^{\circ}\text{C}$, which was mainly due to the decomposition of a large number of heat-labile aliphatic chains. As these side chains contained hydroxyl groups and carbonyl-containing groups, the decomposition generated a large amount of H_2O , CO_2 , CO , etc., resulting in a higher weight loss ratio.

Finally, the third stage, in the range of about 550–800 °C, appeared when most of the oxygen-containing groups cracked and deoxygenated. In this main carbonization stage, the residual substances and C-C and C-H in the benzene ring were further degraded to form charcoal residue through the deprivation of hydrogen [57]. After enzymatic hydrolysis, the weight loss ratio in the first stage of EHCL significantly increased, which was possible because a large number of long branches were destroyed into shorter ones during the enzymatic hydrolysis process with lower thermal stability. At the same time, the weight loss ratio of the second stage was relatively lower than that of CL. In addition, the carbonization stage of EHCL advanced; two weight loss peaks corresponding with the pyrolysis appeared on the DTG curve of EHCL and a weak deep carbonization peak was found at about 800 °C. All the changes in the TG and DTG curves demonstrated that the enzymatic modification of CL could promote carbonation.

The crystal structures of the CL- and EHCL-derived hydrochars were compared with an XRD analysis. Figure 3d shows the XRD patterns of the above two hydrochars. Both of them showed broad amorphous carbon and sharp graphitized carbon diffraction peaks at around 23° (002) and 44° (100) [58]. The peak at 23° of EHCL shifted to a lower diffraction angle compared with that of CL, which proved that the interlayer spacing of the carbon layer increased, possibly resulting from the doping of N elements during the enzymatic hydrolysis process. The crystal structures of the two hydrochars were further proved by Raman spectroscopy. As shown in Figure 3e, the Raman spectra of the two hydrochars both showed D and G peaks at about 1345 and 1580 cm⁻¹, corresponding with disordered and graphitized carbon, respectively [59]. It was calculated that the value of ID/IG reduced from 1.1 of CL to 0.96 of EHCL, indicating that enzymatic modification could increase the graphitization degree of carbon materials due to the lower molecular weight and distribution of EHCL [60].

The structural differences between the CL- and EHCL-derived hydrochars were further compared by nitrogen adsorption–desorption isotherm experiments, and the results are shown in Figure 3f. It could be seen that both carbon materials showed typical type II adsorption isotherms with a lower N₂ adsorption quantity, according to the IUPAC classification. In the low-pressure region of $p/p_0 < 0.01$, the sharp increment in the slope of the curves suggested that there were a certain number of micropores in both carbon materials. A hysteresis loop was observed in the region of p/p_0 of 0.4~0.6 without limiting adsorption in the high-pressure region, indicating the formation of mesopores and macropores. Remarkably, the larger hysteresis loop of EHCL indicated that the carbon skeleton structure was looser, and more mesopores and macropores were associated with the EHCL-derived carbon material. The EHCL-derived carbon material exhibited a higher SSA than that of CL (Table 1), and the BET SSA increased from 194 to 307 m²/g. In addition, it was found that enzymatic hydrolysis could simultaneously increase the micropores and mesopores as well as the average pore size.

Table 1. Porosity characteristics of different carbon materials.

Sample	S _{BET} (m ² /g)	V _{total} (cm ³ /g)	V _{micro} (m ³ /g)	V _{meso} (m ³ /g)	V _{micro} /V _{total} (%)	D (nm)
CL	194	0.11	0.08	0.01	73	2.97
EHCL	307	0.18	0.13	0.03	72	3.94
EHCL-Ka	779	0.51	0.25	0.02	49	3.73
EHCL-Kb	1576	0.62	0.38	0.05	61	2.88
EHCL-Kc	1605	0.81	0.56	0.08	69	3.10
EHCL-Kd	1771	1.17	0.74	0.12	73	3.22
CL-K	1217	0.53	0.33	0.06	62	2.18

Under the same carbonization conditions, the effect of enzymatic hydrolysis on carbonization products was compared (Figure 4). The XRD and Raman spectra showed the amorphous structure of the two samples (Figure 4a,b). It can be seen from Figure 3c that EHCL-Kd exhibited a smaller average particle size than CL-K, which was consistent with

the SEM results. The difference between the structure of EHCL-Kd and CL-K was revealed by adsorption–desorption isotherms (Figure 4d). The isotherm curve of CL-K exhibited a type IV hysteresis loop without an apparent saturated adsorption plateau, corresponding with the irregular pore structure. The XRD and Raman results were also in accordance with the SEM images. Moreover, CL-K owned a lower quantity of absorbed product, suggesting that the SSA was lower than that of EHCL-Kd (Table 1). Conversely, EHCL-Kd transformed into a type I isotherm with a higher adsorption capacity, which was due to the more regular honeycomb-like pore structure with hierarchical porosity (Figure 1k,l).

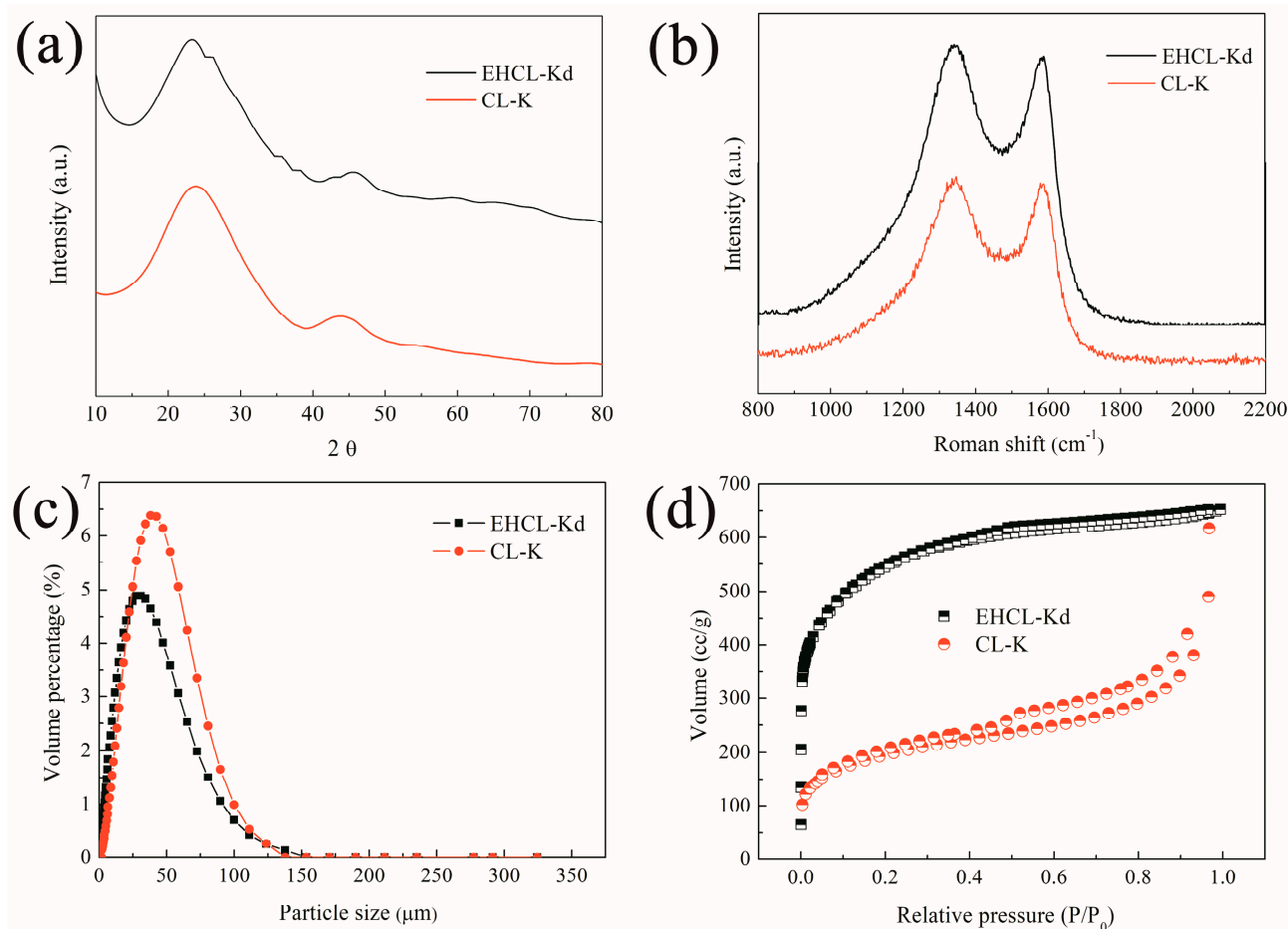


Figure 4. (a) XRD patterns; (b) Raman spectra; (c) particle size distribution; and (d) N_2 adsorption–desorption isotherms of CL-K and EHCL-Kd.

The effect of the KOH/EHCL feed ratio on the structure of EHCL-derived PCs was also researched. Figure 5a shows the XRD patterns of the PCs in the wide-angle region under different KOH/EHCL feed ratios, and all spectra showed amorphous and graphitized carbon diffraction peaks at 22° (002) and 44° (100), as expected. However, the diffraction peak intensity at 44° was markedly decreased when compared with that of the EHCL-derived carbon materials, which may have been due to the increase in disorder resulting from the formation of micropores by KOH activation. Increasing the KOH/EHCL feed ratio gradually enhanced the peak intensity at 44° , which increased the graphitization degree. The structure of the EHCL-derived PCs was further confirmed by Raman spectroscopy (Figure 5b). D and G peaks appeared at 1330 and 1560 cm^{-1} in all spectra, corresponding with disordered carbon and SP^2 -hybridized graphitized carbon, respectively. Meanwhile, with the increase in KOH dosage, the I_D/I_G decreased from 0.98 to 0.91, confirming that the graphitization degree gradually increased. The collapse and rearrangement of

a framework during pyrolysis is beneficial to improve the graphitization degree and the electrical conductivity of PCs.

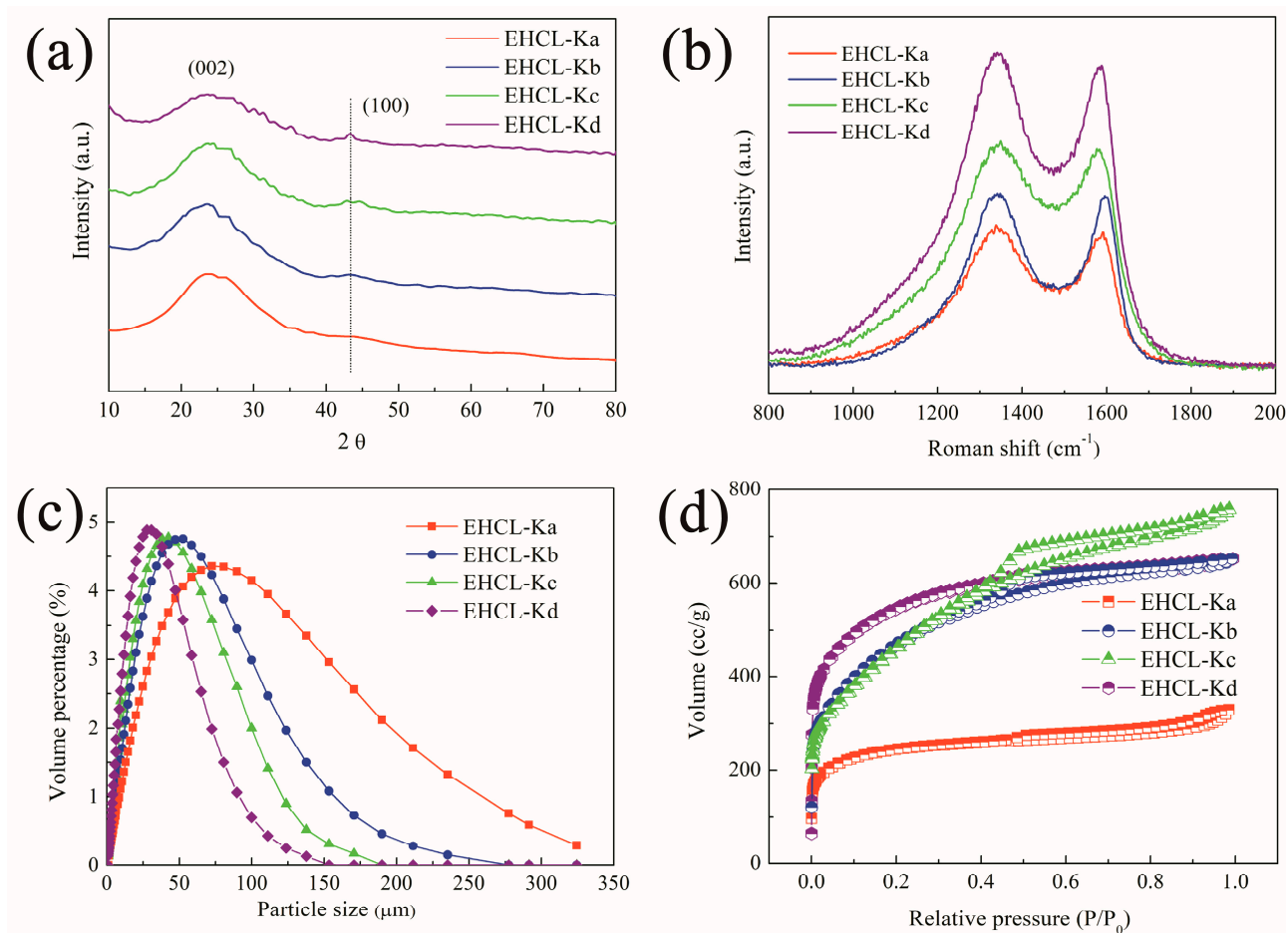


Figure 5. (a) XRD patterns; (b) Raman spectra; (c) particle size distribution; and (d) N_2 adsorption–desorption isotherms of EHCL-Ks.

Figure 5c shows the particle size distribution of different PCs. When increasing the KOH dosage, the particle size distribution of carbon materials significantly decreased with a gradual increase in the pore volume, which was beneficial to improve the contact area between the electrode and electrolyte, promoting the diffusion of ions in the internal pores of the electrode. The diversity in the structure of PCs under different KOH dosages was further revealed by nitrogen adsorption technology.

Figure 5d shows the isotherm nitrogen adsorption–desorption curves of different PCs, and the relevant pore data are listed in Table 1. Compared with the EHCL-derived carbon materials, the KOH activation significantly increased the N_2 adsorption capacity, and the curve gradually transformed from type II to type IV, and finally to type I, with evident plateaus with the increase in the KOH/EHCL feed ratio. It suggested that KOH could increase the content of pores, especially the micropore content in carbon materials. As the amount of KOH increased, some micropores were squeezed and deformed, and collapsed by the nearby macropores or mesopores due to the uneven pore size distribution, causing the curve to transform into a type IV characteristic. When the amount of KOH was further increased, the adsorption capacity of the curve in the low-pressure region ($p/p_0 < 0.01$) significantly increased, proving that the proportion of microporous structures in the PCs was further increased. The relatively uniform distribution could stabilize the micropore so that it was not prone to collapse, which corresponded with the characteristics of type I. It can also be seen from Table 1 that the BET SSA and pore volume increased from

779 m²/g and 0.51 cm³/g to 1771 m²/g and 1.17 cm³/g, respectively, with the increase in the KOH/EHCL ratio. EHCL-Kd showed the highest contents of the total pore, micropore, and mesopore volume than the others, in which the increased mesopore number facilitated the diffusion of ions through the pores [61].

The electrochemical performances of EHCL-based PC electrodes were investigated by a three-electrode configuration, and CV, GCD, and EIS tests were performed in a 6 M KOH aqueous solution. The CV curves of carbon material electrodes at different KOH/EHCL feed ratios are shown in Figure 6a; all the curves showed a similar rectangular shape, with broadening oxidation-reduction peaks appearing in the range of −0.9 to −0.3 v. The above results implied that the EHCL-derived PC electrodes were dominated by EDLC behavior, whilst the corresponding pseudocapacitive behavior was caused by some oxygen-containing functional groups [62]. Among all samples, the CV curve of EHCL-Kd showed the largest area, indicating the best capacitance performance. This was mainly attributed to EHCL-Kd exhibiting the largest SSA, with a unique hierarchical pore size distribution, higher mesopore volume, and an appropriate graphitization degree. Figure 6b shows the GCD curves of different PC electrodes; all curves were approximately isosceles triangles, which further proved the dominating EDLC behavior. Unlike the charging process, the discharge lines of all samples were not perfectly linear and the curvature corresponded with a broadening peak in the CV curve. As expected, EHCL-Kd exhibited the longest charge–discharge time at a current density of 1 A/g, which was consistent with the CV test results. Based on Equation (1), the specific capacitance changes of different PC electrodes under different current densities were calculated, according to the corresponding GCD results (Figure 6c). EHCL-Kd exhibited the largest specific capacitance of 147 F/g at 0.25 A/g and maintained 78% of the initial value at 10 A/g, which indicated its excellent rate performance. Electrolyte ions were first stored in the macropores in EHCL-Kd, and then quickly entered the electrode through the mesopores and smooth pore walls [63].

The capacitive behavior of different PC electrodes during charge storage was further tested by EIS (Figure 6d). In the low-frequency region (magnified figure), the EHCL-Kd electrode distinctly exhibited an almost perpendicular line to the real axis, indicating a relatively low mass transfer hindrance. The higher mesoporous ratio became a low-resistance pathway for electrolyte ion diffusion, and the excellent EDLC properties of the electric layer enabled the fast transport of ions in the electrolyte to the inner pores. A smaller semicircle radius of EHCL-Kd in the high-frequency region indicated its lower interfacial charge transfer resistance. The factors affecting ohmic resistance are not only the resistance of the electrolyte, current collector, active material, coin cell, and separator, but also the contact resistance between the current collector and active material, which could be evaluated by the first intercept value on the real axis. It was known from the EIS curves that the ohmic values of the EHCL-based supercapacitors were 0.83, 0.72, 0.62, and 0.51 Ω, respectively. In addition, the equivalent series resistance of different carbon electrodes could be calculated as 3.5, 2.8, 2.5, and 1.4 Ω, respectively, according to the shorter Warburg-type line (45° slope) in the high-frequency region, indicating a faster ion diffusion rate in the EHCL-Kd electrode due to the larger SSA and hierarchical porous structure [64].

The effect of the 3D structure of EHCL-Kd on the electrochemical performance was further confirmed (Figure 7). The CV curves of EHCL-Kd maintained a rectangular-like shape at different scan rates from 10 to 200 mV/s, which indicated the main EDLC characteristics and preferred rate capability. The GCD curves of EHCL-Kd exhibited in Figure 7b showed high linearity and symmetry at different current densities, demonstrating its excellent electrochemical reversibility and coulombic efficiency. As shown in Figure 7c, the cyclic stability of EHCL-Kd was also evaluated by consecutive GCD for 15,000 cycles at 10 A/g. After 15,000 cycles, the specific capacitance maintained 95.3% of the initial value, indicating that the charge–discharge process was highly reversible. The GCD curve remained close to its initial shape after 15,000 cycles, which also indicated high cycle durability. In Figure 7d, when using EHCL-Kd as the electrode in an aqueous electrolyte

for the symmetric supercapacitor, the highest energy density was 3.3 Wh/kg at a power density of 25 W/kg, and maintained 2.0 Wh/kg at 2 kW/kg.

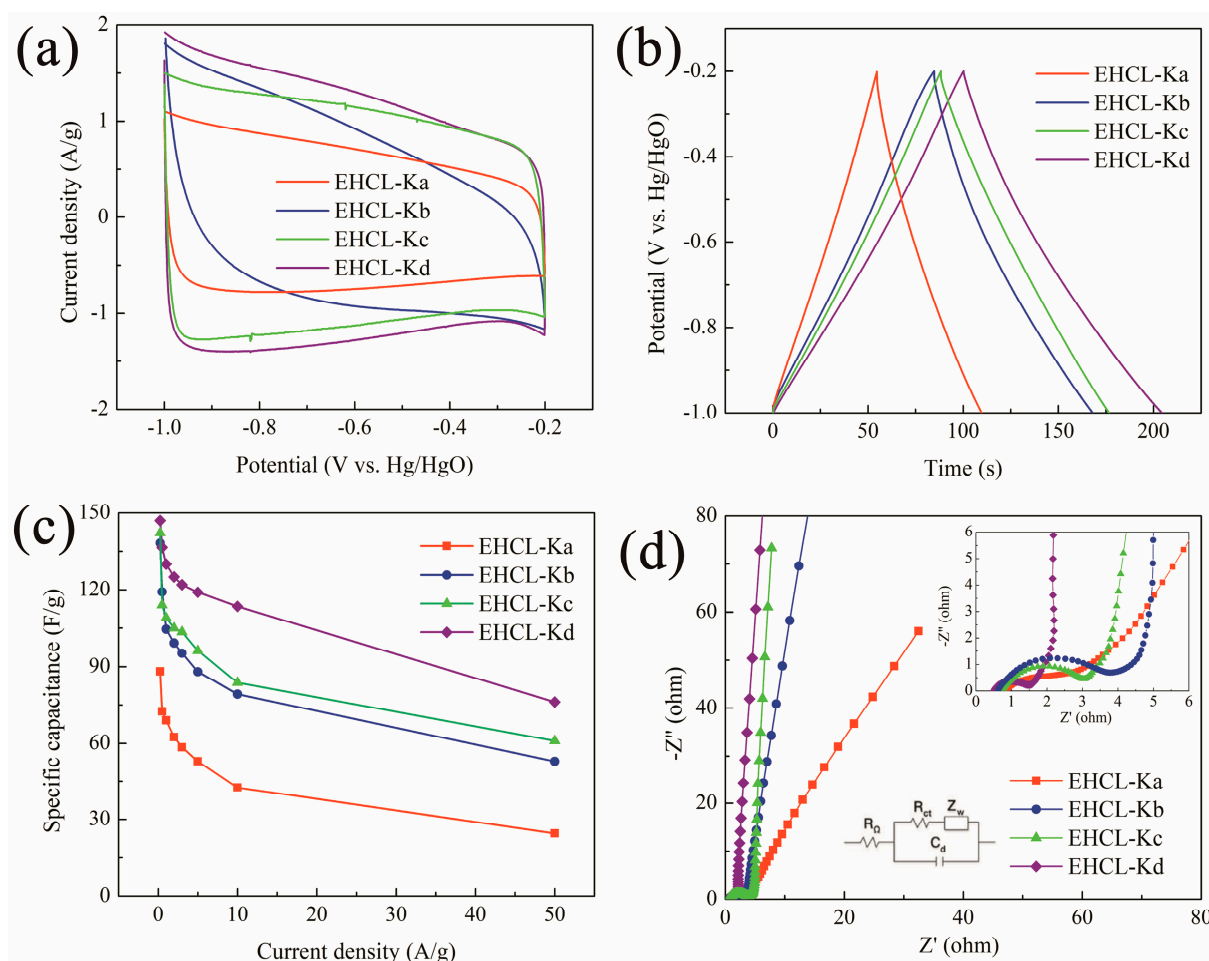


Figure 6. (a) CV curves at 100 mV/s; (b) GCD curves at 1 A/g; (c) rate performance in a three-electrode system in 6 M KOH; and (d) Nyquist plots of EHCL-Ks.

Based on symmetrical two-electrode supercapacitors, the electrochemical properties of the EHCL-Kd electrode were also evaluated (Figure 8). In the scanning rate range of 10–200 mVs, the CV curve of the device based on EHCL-Kd had a symmetrical rectangular shape. At the same time, due to its good capacitance behavior and rate performance, the current response rate of the device was faster when the voltage was reversed (Figure 8a). As shown in Figure 8b, when the current density gradually increased from 0.5 A/g to 10 A/g, the GCD curve of the device presented approximate isosceles triangles, which further reflected its excellent capacitance performance. Figure 8c shows the cyclic stability of the device. As expected, after 10,000 cycles, the GC curve had no obvious change and its specific capacitance retention rate remained above 98%, which further proved the cyclic stability of the device.

The corresponding electrochemical performances of CL-K were carried out to compare them with those of EHCL-Kd (Figure S2). The irregular hole structure and lower SSA of CL-K led to a poor electrochemical performance. These results strongly suggested that enzymatic hydrolysis combined with the alkaline activation method was an essential step to convert CL into 3D hierarchical PCs for high-performance supercapacitor electrodes. Furthermore, the above electrochemical properties were compared with those of the reported biochar electrodes in a three-electrode system, and are summarized in Table 2 [65–69]. It

was found that, in terms of specific capacitance, rate performance, and cycle stability, our work was superior to that of other reported bio-based carbon material electrodes.

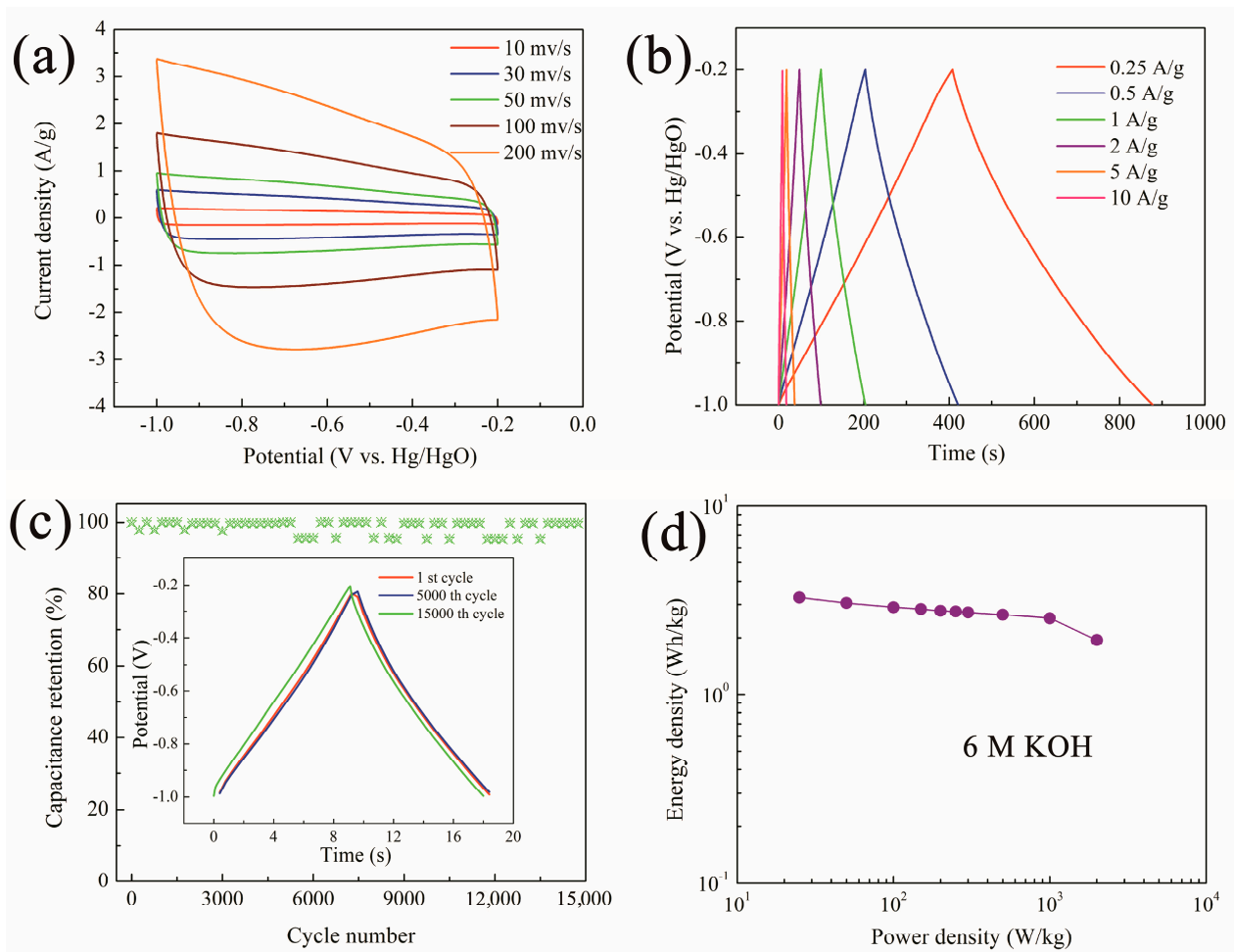


Figure 7. (a) CV curves, (b) GCD curves, and (c) the long-term durability of the EHCL-Kd electrode in a three-electrode system in 6 M KOH (the inset shows the GCD lines of the 1st, 5000th, and 15,000th cycle); (d) Ragone plots for the EHCL-Kd-based supercapacitors.

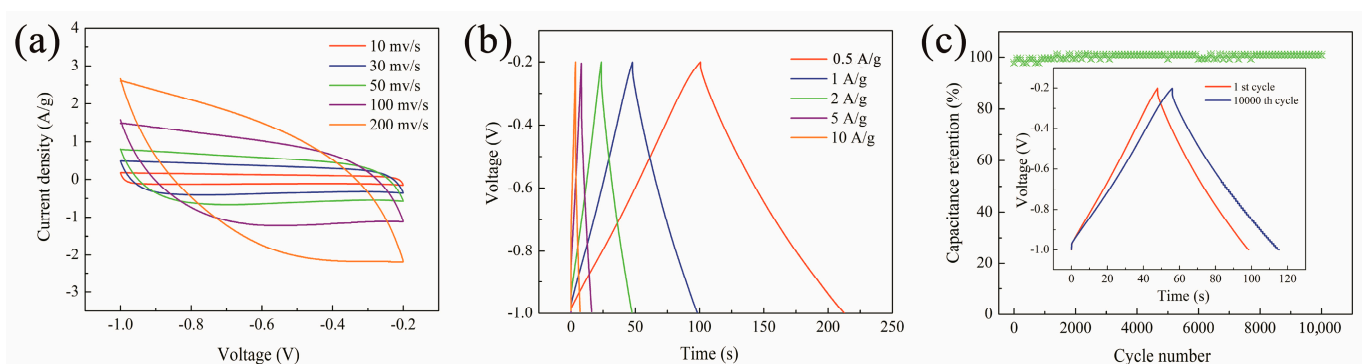


Figure 8. (a) CV curves, (b) GCD curves, and (c) the long-term durability of the EHCL-Kd electrode in a two-electrode system in 6 M KOH (the inset shows the GCD lines of the 1st and 10,000th cycle).

Table 2. Comparison of capacitive performance of EHCL in a three-electrode system.

Biomass Precursor	Current Density (A/g)	Capacitance (F/g)	Rate Capability	Capacitance Retention	Ref.
Sugarcane bagasse	0.5	142	63.4% (10 A/g)	93.9 (5000 cycles at 10 A/g)	[65]
Lignin	0.5	129	84% (5 A/g)	99% (10,000 cycles at 5 A/g)	[66]
Redcedar wood	0.5	115	96% (2.5 A/g)	>90% (5000 cycles at 10 A/g)	[67]
Millet straw	0.2	144	68% (2 A/g)	>95% (10,000 cycles at 10 A/g)	[68]
Wood	0.05	101	42% (10 A/g)	85% (10,000 cycles at 10 A/g)	[69]
EHCL	0.25	147	78% (10 A/g)	95.3% (15,000 cycles at 10 A/g)	This work

4. Conclusions

Several 3D hierarchical PCs were prepared by a low-cost and template-free method using CL as the precursor. Enzymatic hydrolysis depolymerized the macromolecular CL, promoting carbon formation and increasing the SSA and graphitization degree of the carbon materials. Alkali activation enabled the carbonized products to exhibit a unique honeycomb-like 3D hierarchical nanoporous structure whilst significantly increasing the SSA, micropore, and mesopore content. The obtained EHCL-Kd (mass ratio of KOH/EHCL = 3/2) possessed the highest SSA (1771 m²/g), hierarchical porous structure, and good electrochemical performance. Based on the above structural advantages, the EHCL-Kd electrode exhibited a high capacitance (147 F/g at 0.25 A/g), significant rate capability (capacitance retention of 78% at 10 A/g), and good long-term cycling stability, with a capacitance retention of 95.3% after 15,000 cycles in a 6 M KOH aqueous electrolyte. This study demonstrated that the combination of enzymatic hydrolysis and alkali activation may be a promising route to apply renewable lignin derivatives in high-performance supercapacitors.

Supplementary Materials: The following supporting information can be downloaded at: <https://www.mdpi.com/article/10.3390/en16093824/s1>, Figure S1: GPC curves of CL and EHCL; Figure S2: (a) CV curves at 100 mV/s, (b) GCD curves at 1A/g, (c) rate performance in a three-electrode system in 6 M KOH and (d) Nyquist plots of CL-K and EHCL-Kd.

Author Contributions: Conceptualization, X.Z. and S.L.; Formal Analysis, X.Z. and Y.Z.; Funding Acquisition, J.L.; Investigation, S.L. and Y.Z.; Methodology, H.Y.; Project Administration, J.L.; Resources, J.L.; Validation, X.Z.; Writing—Original Draft, X.Z. and Y.Z.; Writing—Review and Editing, J.L., H.Y. and S.L. All authors have read and agreed to the published version of the manuscript.

Funding: This research was funded by the Jiangsu Key Laboratory of Environmentally Friendly Polymeric Materials (PML2003), The Top-Notch Academic Programs Project of Jiangsu Higher Education Institutions (TAPP), and The Priority Academic Program Development of Jiangsu Higher Education Institutions (PAPD).

Data Availability Statement: Not applicable.

Conflicts of Interest: The authors declare no conflict of interest.

References

- Liu, C.-F.; Liu, Y.-C.; Yi, T.-Y.; Hu, C.-C. Carbon materials for high-voltage supercapacitors. *Carbon* **2019**, *145*, 529–548. [CrossRef]
- Zhou, Y.; Qi, H.; Yang, J.; Bo, Z.; Huang, F.; Islam, M.S.; Lu, X.; Dai, L.; Amal, R.; Wang, C.H.; et al. Two-birds-one-stone: Multifunctional supercapacitors beyond traditional energy storage. *Energy Environ. Sci.* **2021**, *14*, 1854–1896. [CrossRef]
- Hussain, A.; Arif, S.M.; Aslam, M. Emerging renewable and sustainable energy technologies: State of the art. *Renew. Sust. Energy Rev.* **2017**, *71*, 12–28. [CrossRef]
- Wang, L.; Morabito, M.; Payne, C.T.; Robinson, G. Identifying institutional barriers and policy implications for sustainable energy technology adoption among large organizations in California. *Energy Policy* **2020**, *146*, 111768. [CrossRef]
- Moustakas, K.; Loizidou, M.; Rehan, M.; Nizami, A.S. A review of recent developments in renewable and sustainable energy systems: Key challenges and future perspective. *Renew. Sust. Energy Rev.* **2020**, *119*, 109418. [CrossRef]
- Poonam; Sharma, K.; Arora, A.; Tripathi, S.K. Review of supercapacitors: Materials and devices. *J. Energy Storage* **2019**, *21*, 801–825. [CrossRef]
- Özarslan, S.; Atelge, M.R.; Kaya, M.; Ünal, S. Production of dual functional carbon material from biomass treated with NaOH for supercapacitor and catalyst. *Energy Storage* **2021**, *3*, e257. [CrossRef]

8. Shao, Y.; El-Kady, M.F.; Sun, J.; Li, Y.; Zhang, Q.; Zhu, M.; Wang, H.; Dunn, B.; Kaner, R.B. Design and Mechanisms of Asymmetric Supercapacitors. *Chem. Rev.* **2018**, *118*, 9233–9280. [[CrossRef](#)] [[PubMed](#)]
9. Gou, G.; Huang, F.; Jiang, M.; Li, J.; Zhou, Z. Hierarchical porous carbon electrode materials for supercapacitor developed from wheat straw cellulosic foam. *Renew. Energy* **2020**, *149*, 208–216. [[CrossRef](#)]
10. Shah, S.A.R.; Naqvi, S.A.A.; Riaz, S.; Anwar, S.; Abbas, N. Nexus of biomass energy, key determinants of economic development and environment: A fresh evidence from Asia. *Renew. Sustain. Energy Rev.* **2020**, *133*, 110244. [[CrossRef](#)]
11. Wang, F.; Wu, X.; Yuan, X.; Liu, Z.; Zhang, Y.; Fu, L.; Zhu, Y.; Zhou, Q.; Wu, Y.; Huang, W. Latest advances in supercapacitors: From new electrode materials to novel device designs. *Chem. Soc. Rev.* **2017**, *46*, 6816–6854. [[CrossRef](#)] [[PubMed](#)]
12. Miao, L.; Song, Z.; Zhu, D.; Li, L.; Gan, L.; Liu, M. Recent advances in carbon-based supercapacitors. *Mater. Adv.* **2020**, *1*, 945–966. [[CrossRef](#)]
13. Luo, X.-Y.; Chen, Y.; Mo, Y. A review of charge storage in porous carbon-based supercapacitors. *New Carbon Mater.* **2021**, *36*, 49–68. [[CrossRef](#)]
14. Yin, J.; Zhang, W.; Alhebshi, N.A.; Salah, N.; Alshareef, H.N. Synthesis Strategies of Porous Carbon for Supercapacitor Applications. *Small Methods* **2020**, *4*, 1900853. [[CrossRef](#)]
15. Gong, Y.; Li, D.; Fu, Q.; Zhang, Y.; Pan, C. Nitrogen Self-Doped Porous Carbon for High-Performance Supercapacitors. *ACS Appl. Energy Mater.* **2020**, *3*, 1585–1592. [[CrossRef](#)]
16. Zuliani, J.E.; Tong, S.; Jia, C.Q.; Kirk, D.W. Contribution of surface oxygen groups to the measured capacitance of porous carbon supercapacitors. *J. Power Sources* **2018**, *395*, 271–279. [[CrossRef](#)]
17. Li, Z.; Guo, D.; Liu, Y.; Wang, H.; Wang, L. Recent advances and challenges in biomass-derived porous carbon nanomaterials for supercapacitors. *Chem. Eng. J.* **2020**, *397*, 125418. [[CrossRef](#)]
18. Bi, Z.; Kong, Q.; Cao, Y.; Sun, G.; Su, F.; Wei, X.; Li, X.; Ahmad, A.; Xie, L.; Chen, C.-M. Biomass-derived porous carbon materials with different dimensions for supercapacitor electrodes: A review. *J. Mater. Chem. A* **2019**, *7*, 16028–16045. [[CrossRef](#)]
19. Niu, W.; Xiao, Z.; Wang, S.; Zhai, S.; Qin, L.; Zhao, Z.; An, Q. Synthesis of nickel sulfide-supported on porous carbon from a natural seaweed-derived polysaccharide for high-performance supercapacitors. *J. Alloys Compd.* **2021**, *853*, 157123. [[CrossRef](#)]
20. Hu, Y.; Xie, K.; Wang, H.; Yuan, C.; Cao, B.; Qian, L.; Wang, S.; Fazeli Zafar, F.; Ding, K.; Wang, Q. Preparation and property of N-doped porous carbon material by one-step pyrolysis of protein-rich algal biomass. *J. Anal. Appl. Pyrolysis* **2021**, *157*, 105221. [[CrossRef](#)]
21. Zheng, S.; Zhang, J.; Deng, H.; Du, Y.; Shi, X. Chitin derived nitrogen-doped porous carbons with ultrahigh specific surface area and tailored hierarchical porosity for high performance supercapacitors. *J. Bioresour. Bioprod.* **2021**, *6*, 142–151. [[CrossRef](#)]
22. Xiao, J.; Li, H.; Zhang, H.; He, S.; Zhang, Q.; Liu, K.; Jiang, S.; Duan, G.; Zhang, K. Nanocellulose and its derived composite electrodes toward supercapacitors: Fabrication, properties, and challenges. *J. Bioresour. Bioprod.* **2022**, *7*, 245–269. [[CrossRef](#)]
23. Yan, B.; Feng, L.; Zheng, J.; Zhang, Q.; Jiang, S.; Zhang, C.; Ding, Y.; Han, J.; Chen, W.; He, S. High performance supercapacitors based on wood-derived thick carbon electrodes synthesized via green activation process. *Inorg. Chem. Front.* **2022**, *9*, 6108–6123. [[CrossRef](#)]
24. Liao, J.J.; Latif, N.H.A.; Trache, D.; Brosse, N.; Hussin, M.H. Current advancement on the isolation, characterization and application of lignin. *Int. J. Biol. Macromol.* **2020**, *162*, 985–1024. [[CrossRef](#)] [[PubMed](#)]
25. Meng, Y.; Lu, J.; Cheng, Y.; Li, Q.; Wang, H. Lignin-based hydrogels: A review of preparation, properties, and application. *Int. J. Biol. Macromol.* **2019**, *135*, 1006–1019. [[CrossRef](#)] [[PubMed](#)]
26. Neiva, D.M.; Rencoret, J.; Marques, G.; Gutiérrez, A.; Gominho, J.; Pereira, H.; del Río, J.C. Lignin from Tree Barks: Chemical Structure and Valorization. *ChemSusChem* **2020**, *13*, 4537–4547. [[CrossRef](#)]
27. Yang, H.; Yu, B.; Xu, X.; Bourbigot, S.; Wang, H.; Song, P. Lignin-derived bio-based flame retardants toward high-performance sustainable polymeric materials. *Green Chem.* **2020**, *22*, 2129–2161. [[CrossRef](#)]
28. Liang, D.; Zhu, X.; Dai, P.; Lu, X.; Guo, H.; Que, H.; Wang, D.; He, T.; Xu, C.; Robin, H.M.; et al. Preparation of a novel lignin-based flame retardant for epoxy resin. *Mater. Chem. Phys.* **2021**, *259*, 124101. [[CrossRef](#)]
29. Supanchaiyamat, N.; Jetsrisuparb, K.; Knijnenburg, J.T.N.; Tsang, D.C.W.; Hunt, A.J. Lignin materials for adsorption: Current trend, perspectives and opportunities. *Bioresour. Technol.* **2019**, *272*, 570–581. [[CrossRef](#)]
30. Shao, L.; Liu, N.; Wang, L.; Sang, Y.; Wan, H.A.; Zhan, P.; Zhang, L.; Huang, J.; Chen, J. Facile preparation of oxygen-rich porous polymer microspheres from lignin-derived phenols for selective CO₂ adsorption and iodine vapor capture. *Chemosphere* **2022**, *288*, 132499. [[CrossRef](#)]
31. Wang, D.; Lee, S.H.; Kim, J.; Park, C.B. “Waste to Wealth”: Lignin as a Renewable Building Block for Energy Harvesting/Storage and Environmental Remediation. *ChemSusChem* **2020**, *13*, 2807–2827. [[CrossRef](#)] [[PubMed](#)]
32. Guo, N.; Li, M.; Sun, X.; Wang, F.; Yang, R. Enzymatic hydrolysis lignin derived hierarchical porous carbon for supercapacitors in ionic liquids with high power and energy densities. *Green Chem.* **2017**, *19*, 2595–2602. [[CrossRef](#)]
33. Jian, W.; Zhang, W.; Wu, B.; Wei, X.; Liang, W.; Zhang, X.; Wen, F.; Zhao, L.; Yin, J.; Lu, K.; et al. Enzymatic Hydrolysis Lignin-Derived Porous Carbons through Ammonia Activation: Activation Mechanism and Charge Storage Mechanism. *ACS Appl. Mater. Interfaces* **2022**, *14*, 5425–5438. [[CrossRef](#)] [[PubMed](#)]
34. Yedluri, A.K.; Kim, H.-J. Wearable super-high specific performance supercapacitors using a honeycomb with folded silk-like composite of NiCo₂O₄ nanoplates decorated with NiMoO₄ honeycombs on nickel foam. *Dalton Trans.* **2018**, *47*, 15545–15554. [[CrossRef](#)] [[PubMed](#)]

35. Kumar, Y.A.; Kim, H.-J. Effect of Time on a Hierarchical Corn Skeleton-Like Composite of CoO@ZnO as Capacitive Electrode Material for High Specific Performance Supercapacitors. *Energies* **2018**, *11*, 3285. [[CrossRef](#)]
36. Moniruzzaman, M.; Anil Kumar, Y.; Pallavolu, M.R.; Arbi, H.M.; Alzahmi, S.; Obaidat, I.M. Two-Dimensional Core-Shell Structure of Cobalt-Doped@MnO₂ Nanosheets Grown on Nickel Foam as a Binder-Free Battery-Type Electrode for Supercapacitor Application. *Nanomaterials* **2022**, *12*, 3187. [[CrossRef](#)]
37. Schütter, C.; Pohlmann, S.; Balducci, A. Industrial Requirements of Materials for Electrical Double Layer Capacitors: Impact on Current and Future Applications. *Adv. Energy Mater.* **2019**, *9*, 1900334. [[CrossRef](#)]
38. Lee, D.-Y.; An, G.-H.; Ahn, H.-J. High-surface-area tofu based activated porous carbon for electrical double-layer capacitors. *J. Ind. Eng. Chem.* **2017**, *52*, 121–127. [[CrossRef](#)]
39. Wei, J.; Li, Y.; Dai, D.; Zhang, F.; Zou, H.; Yang, X.; Ji, Y.; Li, B.; Wei, X. Surface Roughness: A Crucial Factor To Robust Electric Double Layer Capacitors. *ACS Appl. Mater. Interfaces* **2020**, *12*, 5786–5792. [[CrossRef](#)]
40. Karaman, C.; Karaman, O.; Atar, N.; Yola, M.L. Sustainable electrode material for high-energy supercapacitor: Biomass-derived graphene-like porous carbon with three-dimensional hierarchically ordered ion highways. *Phys. Chem. Chem. Phys.* **2021**, *23*, 12807–12821. [[CrossRef](#)]
41. Luo, H.; Lu, H.; Qiu, J. Carbon fibers surface-grown with helical carbon nanotubes and polyaniline for high-performance electrode materials and flexible supercapacitors. *J. Electroanal. Chem.* **2018**, *828*, 24–32. [[CrossRef](#)]
42. Shao, F.; Bian, S.-W.; Zhu, Q.; Guo, M.-X.; Liu, S.; Peng, Y.-H. Fabrication of Polyaniline/Graphene/Polyester Textile Electrode Materials for Flexible Supercapacitors with High Capacitance and Cycling Stability. *Chem.-Asian J.* **2016**, *11*, 1906–1912. [[CrossRef](#)] [[PubMed](#)]
43. Li, J.; Qiu, S.; Liu, B.; Chen, H.; Xiao, D.; Li, H. Strong interaction between polyaniline and carbon fibers for flexible supercapacitor electrode materials. *J. Power Sources* **2021**, *483*, 229219. [[CrossRef](#)]
44. Cai, Y.; Luo, Y.; Dong, H.; Zhao, X.; Xiao, Y.; Liang, Y.; Hu, H.; Liu, Y.; Zheng, M. Hierarchically porous carbon nanosheets derived from *Moringa oleifera* stems as electrode material for high-performance electric double-layer capacitors. *J. Power Sources* **2017**, *353*, 260–269. [[CrossRef](#)]
45. Schwieger, W.; Machoke, A.G.; Weissenberger, T.; Inayat, A.; Selvam, T.; Klumpp, M.; Inayat, A. Hierarchy concepts: Classification and preparation strategies for zeolite containing materials with hierarchical porosity. *Chem. Soc. Rev.* **2016**, *45*, 3353–3376. [[CrossRef](#)]
46. Liu, X.; Liu, X.; Sun, B.; Zhou, H.; Fu, A.; Wang, Y.; Guo, Y.-G.; Guo, P.; Li, H. Carbon materials with hierarchical porosity: Effect of template removal strategy and study on their electrochemical properties. *Carbon* **2018**, *130*, 680–691. [[CrossRef](#)]
47. Cai, G.; Yan, P.; Zhang, L.; Zhou, H.-C.; Jiang, H.-L. Metal–Organic Framework-Based Hierarchically Porous Materials: Synthesis and Applications. *Chem. Rev.* **2021**, *121*, 12278–12326. [[CrossRef](#)]
48. Gao, F.; Zang, Y.-H.; Wang, Y.; Guan, C.-Q.; Qu, J.-Y.; Wu, M.-B. A review of the synthesis of carbon materials for energy storage from biomass and coal/heavy oil waste. *New Carbon Mater.* **2021**, *36*, 34–48. [[CrossRef](#)]
49. Guan, T.; Zhao, J.; Zhang, G.; Wang, J.; Zhang, D.; Li, K. Template-Free Synthesis of Honeycomblike Porous Carbon Rich in Specific 2–5 nm Mesopores from a Pitch-Based Polymer for a High-Performance Supercapacitor. *ACS Sustain. Chem. Eng.* **2019**, *7*, 2116–2126. [[CrossRef](#)]
50. Jeon, J.-W.; Zhang, L.; Lutkenhaus, J.L.; Laskar, D.D.; Lemmon, J.P.; Choi, D.; Nandasiri, M.I.; Hashmi, A.; Xu, J.; Motkuri, R.K.; et al. Controlling Porosity in Lignin-Derived Nanoporous Carbon for Supercapacitor Applications. *ChemSusChem* **2015**, *8*, 428–432. [[CrossRef](#)]
51. Li, H.; Yuan, D.; Tang, C.; Wang, S.; Sun, J.; Li, Z.; Tang, T.; Wang, F.; Gong, H.; He, C. Lignin-derived interconnected hierarchical porous carbon monolith with large areal/volumetric capacitances for supercapacitor. *Carbon* **2016**, *100*, 151–157. [[CrossRef](#)]
52. Si, M.; Yan, X.; Liu, M.; Shi, M.; Wang, Z.; Wang, S.; Zhang, J.; Gao, C.; Chai, L.; Shi, Y. In Situ Lignin Bioconversion Promotes Complete Carbohydrate Conversion of Rice Straw by *Cupriavidus basilensis* B-8. *ACS Sustain. Chem. Eng.* **2018**, *6*, 7969–7978. [[CrossRef](#)]
53. Liu, Y.; Huang, G.; Li, Y.; Yao, Y.; Zhang, F.; Xing, B.; Zhang, C. N–O–S Co-doped Hierarchical Porous Carbons Derived from Calcium Lignosulfonate for High-Performance Supercapacitors. *Energy Fuels* **2020**, *34*, 3909–3922. [[CrossRef](#)]
54. Huang, G.; Liu, Y.; Chen, H.; Xing, B.; Li, Y.; Yao, Y.; Jia, J.; Liu, Q.; Zhang, C. A novel grafting-template method to prepare three-dimensional hierarchical porous carbon with high surface area and electrical conductivity for superior-performance supercapacitors. *J. Power Sources* **2021**, *482*, 228922. [[CrossRef](#)]
55. Shi, F.; Tong, Y.; Li, H.; Li, J.; Cong, Z.; Zhai, S.; An, Q.; Wang, K. Synthesis of oxygen/nitrogen/sulfur codoped hierarchical porous carbon from enzymatically hydrolyzed lignin for high-performance supercapacitors. *J. Energy Storage* **2022**, *52*, 104992. [[CrossRef](#)]
56. Yang, H.; Yan, R.; Chen, H.; Lee, D.H.; Zheng, C. Characteristics of hemicellulose, cellulose and lignin pyrolysis. *Fuel* **2007**, *86*, 1781–1788. [[CrossRef](#)]
57. Zhou, H.; Long, Y.; Meng, A.; Li, Q.; Zhang, Y. The pyrolysis simulation of five biomass species by hemi-cellulose, cellulose and lignin based on thermogravimetric curves. *Thermochim. Acta* **2013**, *566*, 36–43. [[CrossRef](#)]
58. Woo, S.-W.; Dokko, K.; Nakano, H.; Kanamura, K. Preparation of three dimensionally ordered macroporous carbon with mesoporous walls for electric double-layer capacitors. *J. Mater. Chem.* **2008**, *18*, 1674–1680. [[CrossRef](#)]

59. Yoo, E.; Nakamura, J.; Zhou, H. N-Doped graphene nanosheets for Li–air fuel cells under acidic conditions. *Energy Environ. Sci.* **2012**, *5*, 6928–6932. [[CrossRef](#)]
60. Zhang, K.; Liu, M.; Zhang, T.; Min, X.; Wang, Z.; Chai, L.; Shi, Y. High-performance supercapacitor energy storage using a carbon material derived from lignin by bacterial activation before carbonization. *J. Mater. Chem. A* **2019**, *7*, 26838–26848. [[CrossRef](#)]
61. Li, Y.; Li, Z.; Shen, P.K. Simultaneous Formation of Ultrahigh Surface Area and Three-Dimensional Hierarchical Porous Graphene-Like Networks for Fast and Highly Stable Supercapacitors. *Adv. Mater.* **2013**, *25*, 2474–2480. [[CrossRef](#)] [[PubMed](#)]
62. Wang, K.; Yan, R.; Zhao, N.; Tian, X.; Li, X.; Lei, S.; Song, Y.; Guo, Q.; Liu, L. Bio-inspired hollow activated carbon microtubes derived from willow catkins for supercapacitors with high volumetric performance. *Mater. Lett.* **2016**, *174*, 249–252. [[CrossRef](#)]
63. Wang, K.; Meng, Q.; Zhang, Y.; Wei, Z.; Miao, M. High-Performance Two-Ply Yarn Supercapacitors Based on Carbon Nanotubes and Polyaniline Nanowire Arrays. *Adv. Mater.* **2013**, *25*, 1494–1498. [[CrossRef](#)] [[PubMed](#)]
64. Wang, H.; Xu, Z.; Kohandehghan, A.; Li, Z.; Cui, K.; Tan, X.; Stephenson, T.J.; King'ondo, C.K.; Holt, C.M.B.; Olsen, B.C.; et al. Interconnected Carbon Nanosheets Derived from Hemp for Ultrafast Supercapacitors with High Energy. *ACS Nano* **2013**, *7*, 5131–5141. [[CrossRef](#)]
65. Hao, P.; Zhao, Z.; Tian, J.; Li, H.; Sang, Y.; Yu, G.; Cai, H.; Liu, H.; Wong, C.P.; Umar, A. Hierarchical porous carbon aerogel derived from bagasse for high performance supercapacitor electrode. *Nanoscale* **2014**, *6*, 12120–12129. [[CrossRef](#)] [[PubMed](#)]
66. Park, J.H.; Rana, H.H.; Lee, J.Y.; Park, H.S. Renewable flexible supercapacitors based on all-lignin-based hydrogel electrolytes and nanofiber electrodes. *J. Mater. Chem. A* **2019**, *7*, 16962–16968. [[CrossRef](#)]
67. Jiang, J.; Zhang, L.; Wang, X.; Holm, N.; Rajagopalan, K.; Chen, F.; Ma, S. Highly ordered macroporous woody biochar with ultra-high carbon content as supercapacitor electrodes. *Electrochim. Acta* **2013**, *113*, 481–489. [[CrossRef](#)]
68. Ding, Y.; Wang, T.; Dong, D.; Zhang, Y. Using Biochar and Coal as the Electrode Material for Supercapacitor Applications. *Front. Energy Res.* **2020**, *7*, 159. [[CrossRef](#)]
69. Wan, C.; Jiao, Y.; Li, J. Core–shell composite of wood-derived biochar supported MnO₂ nanosheets for supercapacitor applications. *RSC Adv.* **2016**, *6*, 64811–64817. [[CrossRef](#)]

Disclaimer/Publisher's Note: The statements, opinions and data contained in all publications are solely those of the individual author(s) and contributor(s) and not of MDPI and/or the editor(s). MDPI and/or the editor(s) disclaim responsibility for any injury to people or property resulting from any ideas, methods, instructions or products referred to in the content.